



# Fluid–structure interaction modeling of compliant aortic valves using the lattice Boltzmann CFD and FEM methods

Adi Morany<sup>1</sup> · Karin Lavon<sup>1</sup> · Ricardo Gomez Bardon<sup>2</sup> · Brandon Kovarovic<sup>3</sup> · Ashraf Hamdan<sup>4</sup> · Danny Bluestein<sup>3</sup> · Rami Haj-Ali<sup>1,3</sup>

Received: 7 August 2022 / Accepted: 28 December 2022 / Published online: 10 February 2023  
© The Author(s), under exclusive licence to Springer-Verlag GmbH Germany, part of Springer Nature 2023

## Abstract

The lattice Boltzmann method (LBM) has been increasingly used as a stand-alone CFD solver in various biomechanical applications. This study proposes a new fluid–structure interaction (FSI) co-modeling framework for the hemodynamic-structural analysis of compliant aortic valves. Toward that goal, two commercial software packages are integrated using the lattice Boltzmann (LBM) and finite element (FE) methods. The suitability of the LBM-FE hemodynamic FSI is examined in modeling healthy tricuspid and bicuspid aortic valves (TAV and BAV), respectively. In addition, a multi-scale structural approach that has been employed explicitly recognizes the heterogeneous leaflet tissues and differentiates between the collagen fiber network (CFN) embedded within the elastin matrix of the leaflets. The CFN multi-scale tissue model is inspired by monitoring the distribution of the collagen in 15 porcine leaflets. Different simulations have been examined, and structural stresses and resulting hemodynamics are analyzed. We found that LBM-FE FSI approach can produce good predictions for the flow and structural behaviors of TAV and BAV and correlates well with those reported in the literature. The multi-scale heterogeneous CFN tissue structural model enhances our understanding of the mechanical roles of the CFN and the elastin matrix behaviors. The importance of LBM-FE FSI also emerges in its ability to resolve local hemodynamic and structural behaviors. In particular, the diastolic fluctuating velocity phenomenon near the leaflets is explicitly predicted, providing vital information on the flow transient nature. The full closure of the contacting leaflets in BAV is also demonstrated. Accordingly, good structural kinematics and deformations are captured for the entire cardiac cycle.

**Keywords** Lattice Boltzmann method (LBM) · Aortic valve biomechanics · Fluid–structure interaction (FSI) · Finite element (FE)

## 1 Introduction

The aortic valve (AV) is a tricuspid valve in the human heart between the left ventricle and the aorta. A normally functioning aortic valve permits normal physiological function, but its dysfunction may result in several clinical

complications, e.g., left ventricular hypertrophy including dilation, decreased cardiac output, arrhythmias, etc. Bicuspid aortic valve (BAV) is the most common form of congenital heart disease and is found in approximately 0.5–1.4% of the population (Masri et al. 2017). BAV is associated with valvular pathologies such as aortic regurgitation and aortic stenosis (Cedars and Braverman 2012). The AV hemodynamic parameters of normal or pathological function are associated and significantly impact diseases diagnostics and prediction, e.g., dilatation, aneurysm or atherosclerosis (Davies 2009; Dua and Dalman 2010). Over the years, three main simulation methods were used predominantly to present its hemodynamic and structural behavior; structural-only models, computational fluid dynamics (CFD) models and fluid–structure interaction (FSI) models.

Structural-only models are widely used where a trans-valvular pressure difference is applied directly to the AV

✉ Rami Haj-Ali  
rami98@tau.ac.il

<sup>1</sup> School of Mechanical Engineering, Tel Aviv University, Tel Aviv, Israel

<sup>2</sup> Dassault Systemes España, Madrid, Spain

<sup>3</sup> Department of Biomedical Engineering, Stony Brook University, Stony Brook, NY, USA

<sup>4</sup> Department of Cardiology, Rabin Medical Center, Petach Tikva, Faculty of Medicine, Tel Aviv University, Tel Aviv, Israel

cusps, thus neglecting the influence of blood flow. The finite element (FE) method is used extensively in these models. For example, simulating the response of bioprosthetic and polymeric valves to paravalvular pressure gradient (Sun et al. 2005; Liu et al. 2007; Haj-Ali et al. 2008). Conti et al. (2010a, b) compared a TAV model to two identical asymmetric BAV models, with and without a thickened raphe. Jermihov et al. (2011) investigated the impact of different geometric variations of BAV on the stress distribution in the cusps, while created two BAV models with a non-fused cusp (NFC) angle of  $180^\circ$ , of type 0 and 1 and two models with an NFC angle of  $120^\circ$  type 1, with and without raphe and for comparison created a symmetric TAV. Both studies agreed that there were higher stresses in the BAV more than the TAV, while the opening orifice in the BAV was smaller more than that of the TAV. They concluded that the geometrical changes influenced the maximum magnitudes of stress–strain than the material differences.

The CFD models that are broadly used assume a weak or no effect of the dynamic structure. Ge et al. (2003) simulated a 3D rigid valve by assuming that the cusps were fixed for different opening angles. Hellmeier et al. (2018) evaluated biological and mechanical aortic valve prosthesis using patient-specific MRI where Weese et al. (2017) compared ejection fractions and effective orifice area (EOA) for patient anatomies from the heart and aortic valve segmentation of CT.

Fluid–structure interaction models (FSI) have been studied recently. These models consider an elastic structure contacting a flowing fluid that is subjected to a pressure that causes deformation in it. Hence, the deformed structure affects the flow field. The altered flowing fluid, in its turn, exerts another pressure on the structure with repeats of the process. The most used FSI simulations related to AV are Navier–Stokes approach based, such as arbitrary Lagrangian–Eulerian approach, immersed boundary, "Operator Split," fictitious domain method and mesh-free Lagrangian methods as smoothed-particle hydrodynamics (Marom 2015). Models of TAV are primarily concerned with predicting the flow across prosthetic mechanical valves with rigid cusps, in 2D (Rankin et al. 2008) and 3D models (Borazjani et al. 2010) or biological valves (Bongert et al. 2018). In addition, FSI simulations of flexible valves have also been conducted using hyperelastic models (Chen and Luo 2018). Sigüenza et al. (2018) showed experiment vs. simulation comparison of pulsatile flow with an AV model. Few studies have investigated BAV using FSI analysis. Some studies are limited to 2D simulations only. Chandra et al. (2012) created 2D FSI models of TAV and two asymmetric BAVs, with and without calcification. In the BAV, they noticed a strong jet toward the NFC during systole peak, with higher shear stress more than on TAV. Furthermore, the vortices between the sinuses to the leaflets were higher in the fused cusp. Other

3D models as Katayama et al. (2013) created FSI models and compared rare configuration of a symmetric BAV type 1, to a healthy and stenotic TAV. Ghosh et al. (2018) performed a comparative study between transcatheter and surgical valves examining their hemodynamic and kinematic behaviors utilizing FSI. Later, they evaluated transcatheter aortic valve replacement procedure's hemodynamic outcomes during heart beating (Ghosh et al. 2020). Other studies focused on BAV using FSI. Mendi et al. (2020) developed a patient-specific BAV model and compared to 4D MRI, predicting the mechanical and flow-induced stresses. Marom et al. (2012b) focused on tissue mechanics and hemodynamics and compared TAV to symmetric type 0 BAV and to asymmetric type 1 BAV with and without raphe, using FSI models. They noticed that the raphe does not affect the hemodynamics and found increased vortices in the BAV sinuses due to its asymmetric shape and higher flow shear stress. Our group has conducted in recent years, FSI studies of parametric AVs models in several clinical and numerical analyses (Marom et al. 2012a, c, 2013a; Lavon et al. 2018).

Unlike the traditional CFD methods such as the finite difference, the finite volume and the finite element methods, discretizing Navier–Stokes equations on continuous medium, the lattice Boltzmann method (LBM) models the fluid as fictive particles. These particles perform consecutive propagation and collision processes over a discrete lattice grid. LBM has been used to model diverse flows. Recently, a wide range of studies in various fields and applications like magnetohydrodynamics (Martínez et al. 1994), immiscible fluid (Gunstensen et al. 1991), heat transfer problems (Han-Taw and Jae-Yuh 1993) and porous media (Bernsdorf et al. 2000) have been done. Moreover, in biofluid mechanics, several researches were conducted simulating incompressible steady and unsteady 2D and 3D flow using Chapman–Enskog expansion (He and Luo 1997; Lai, Ching-Long Lin 2001), viscous flow in blood vessels (Fang et al. 2002; Liu 2012) and arterial flow simulation (Boyd et al. 2004), thrombosis modeling in intracranial aneurysms (Ouaed et al. 2008) and computational hemodynamics in patients with coarctation of the aorta (Mirzaee et al. 2017). In addition, FSI models coupling LBM with Lagrangian formulation have studied multiphase flow (Dorschner et al. 2018) and polymer filament transport in red blood cell flow (Tan et al. 2018). Following the studies that have been introduced, very few focused on CFD or FSI models of the aortic valve. Pelliccioni et al. (2007) simulated 2D LBM FSI models to study bileaflet and monoleaflet mechanical valves where the valve motion was calculated as a rigid body motion. Fukui and Morinishi (2013) applied the virtual flux method, a tool to describe stationary or moving body shapes, to 2D AV by regularized LBM with large eddy simulation model. They showed an important parameter diagnosing the mechanism of the AV movements and the generation of cardiovascular

diseases such as aortic stenosis which is the vortices' distribution in time and space. Krafczyk et al. (1998) and Yun et al. (2014a, b) elaborated the same to 3D transient physiological flow CFD in fixed geometry bileaflet mechanical heart valve at different opening angles. All the studies gave detailed information about the transient valve dynamic history, resulting stress analysis and temporal shear stress of the same order of magnitude as observed in experiments of similar in vitro flow problem. During the last years, very few researchers have performed a 3D FSI analyses utilizing LBM and FE for aortic valve models. Gao and Zhang (2020), Gao et al. (2019) evaluated the biomechanical states of TAV under left ventricular assist device working modes, and Kim et al. (2020) investigated the effect of an artificial membrane on the valve quicker closure preventing retrograde blood flow.

Evaluating the effect of anisotropic properties modeling in the AV on stress distribution, valve kinematics and hemodynamic behaviors, few studies examined the collagen fiber network specifically using immersed boundary FSI methods. Nestola et al. (2021) compared between isotropic and fiber-reinforced models examining the different valves designs using embedded approach based on the mortar method. They simulated the full dynamics of prosthetic AV to analyze its mechanical and hemodynamic performances. Wu et al. (2018) considered an anisotropic hyperelastic soft tissue with different fiber orientations with immersogeometric FSI and reproduced the anisotropic stress–strain behavior of cross-linked bovine pericardium experimental tests. Lee et al. (2020) validated the anisotropic models for bulk flow rates, pressures, valve open areas and leaflets kinematics using pulse-duplicator system. Moreover, Abbas et al. (2022) reviewed immersed boundary methods for fixed,

moving and combined grids for AV studies during the recent years. None of the previous studies utilized LBM for compliant AV examining its anisotropic properties, structural or hemodynamic responses.

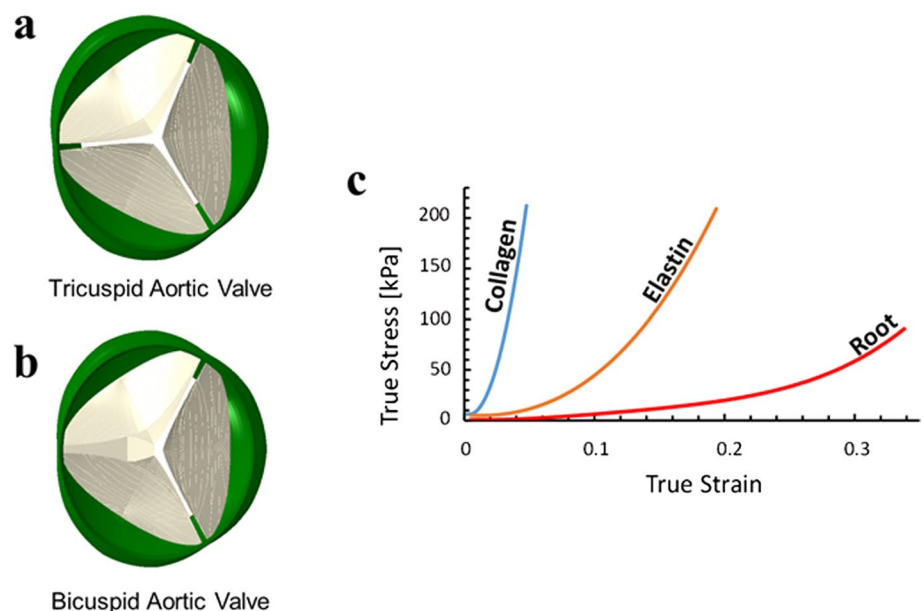
It is evident from the above literature review that AV models have been proposed and extensively investigated. However, most of the FSI models explored the average metrics of the flow and did not consider the instantaneous variations. Moreover, it is essential to develop efficient modeling approaches due to the need for more refined analyses, such as more accurately predict the transient nature of hemodynamic factors, and leaflet deformations and stresses anisotropic behavior. To that end, this study examines a new hemodynamic-structural co-modeling approach using LBM-FE to investigate healthy and pathological aortic valves under physiological pressure conditions. Various parameters have been examined, such as effective orifice area, hemodynamic metrics and stresses distributions, and were compared to available data from the literature.

## 2 Methods

### 2.1 Aortic valve geometry and structural model

The parametric geometry of the AV was constructed based on a previously conducted study by our group (Haj-Ali et al. 2012). The model describes a 3D geometry of TAV and extended to simulating a BAV, including the cusps and the root, identifying and presenting the main curves and surfaces used to reconstruct the valve geometry (Fig. 1a, b). For biomechanical modeling, the annulus diameter was chosen to be 24 mm where any other parameters depend on it. A mesh

**Fig. 1** **a** TAV parametric multi-scale model geometry with embedded collagen fiber network, **b** BAV with 140° non-fused cup angle and embedded collagen fiber network parametric multiscale model geometry, **c** calibrated hyperelastic material properties of the aortic root, cusps and the collagen fiber network



refinement study of the FE structure model was conducted for the root and cusps for shell elements by comparing the solutions of a coarse (14,300 nodes) and fine mesh (125,000 nodes) (Marom et al. 2012a). Briefly, the evolution of the radial and axial displacements at the middle point of the free edge of a leaflet, the maximal principal stress and strain, was investigated under a pressure ramp on the leaflets. The maximal difference found to be less than 10%. Given that, the shell elements of the coarser mesh were extruded into 3D elements. This structure mesh was employed in all the simulations where a 3D linear wedge elements were used with root and cusps thickness of 0.3 and 2 mm, respectively.

The cusps were assumed to have a heterogeneous structure composed of collagen fibers embedded in the elastin matrix. A symmetric averaged collagen fiber network embedded inside the leaflets was mapped and added to the aortic valve parametric model leaflet based on our group's previous study (Marom et al. 2013b; Mega et al. 2016) (Fig. 2) and meshed with beam elements with radii varying from 0.1 to 0.4 mm (Fig. 1a, b) (Marom et al. 2012a). The material properties of the root, elastin and collagen were calibrated using the stress–strain curves published by Gundiah et al. (Gundiah et al. 2008) and Missirlis and Chong (1978), respectively (Fig. 2c). Ogden's first-order model was chosen to fit the above material properties best, and a density of 2000 and 1100 kg/m<sup>3</sup> was used for the root and the cusps (including the fibers), respectively. The structural mesh part of the AV for both TAV and BAV models, each includes ~ 30,000 wedge elements and ~ 800 beam elements.

## 2.2 LBM-FE FSI: physical and numerical setups

The LBM approach is well established (Pelliccioni et al. 2007; Macmeccan et al. 2009; Yun et al. 2014a; Dorschner et al. 2018). The LBM algorithm and method are derived

from the Boltzmann transport equation describing the evolution of a rarefied gas employing a one-particle distribution function. In this study, SIMULIA XFlow (Dassault Systemes, Simulia Corp.) commercial code was utilized for the fluid part. The Boltzmann equation is discretized with each discrete velocity direction, statistically deriving the macroscopic variables of mass and momentum. A multi-relaxation time (MRT) collision operator was employed according to central momentum space in a 3D Cartesian velocity set using D3Q27 uniform lattice. The algorithm is based on equilibrium distributions calculated from the macroscopic fields' initial conditions through collision and streaming process (Fig. 3). A summary of the major governing equations and algorithmic implementation of the Boltzmann transport equations is given in Appendix A.

### 2.2.1 Fluid domain

Representative FSI test cases were modeled utilizing the LBM-FE approach in a healthy AV and in a pathological compliant BAV with an NFC angle of 140°, applying physiological pressure conditions. In order to establish the flow path and conditions from the left ventricle downstream and through the ascending aorta upstream, circular and rigid tubes were added from both sides in lengths of ~ 7 cm (approximately 3 × the root's diameter), composing the entire fluid domain. These entry and exit lengths were established to eliminate boundary conditions and pressure waves effects on the region of interest (Fig. 4).

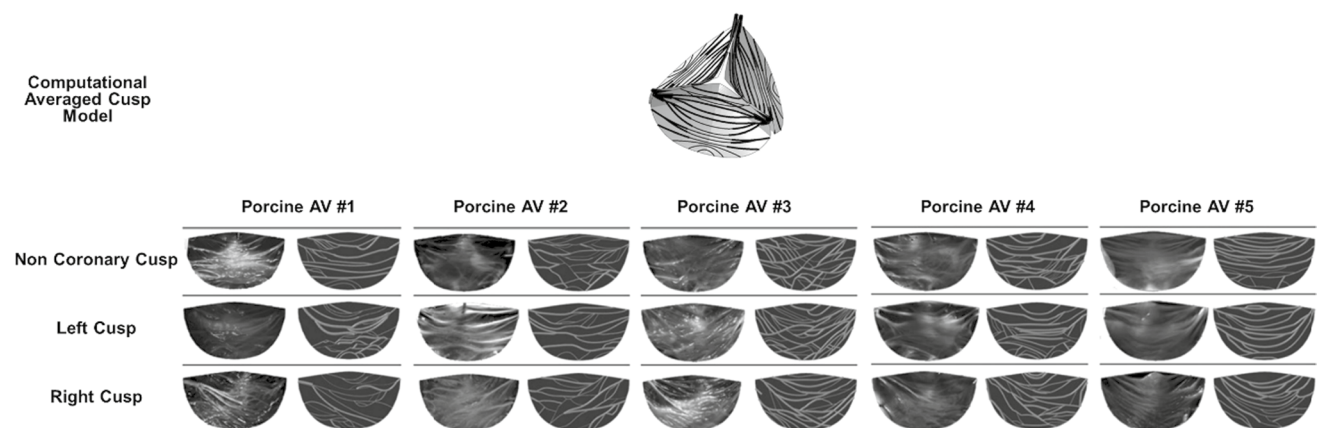


**Fig. 2** Computational averaged collagen fiber symmetric map embedded inside the aortic valve's cusp based on images of right, left and non-coronary cusps from five different porcine valves (Marom et al. 2013b; Mega et al. 2016)

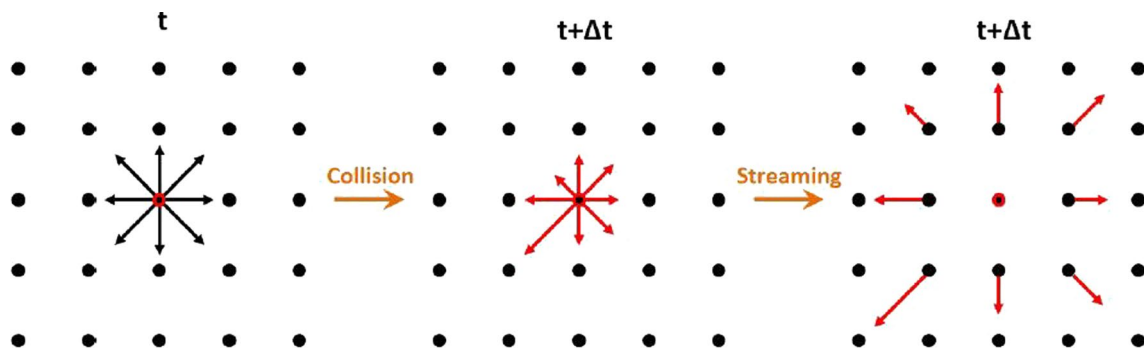


**Fig. 3** Schematic solution procedure of a single-time increment using lattice Boltzmann method. Starting from an equilibrium distribution at the current increment (left). Collision and streaming to the next

time increment (middle). Calculating the new equilibrium distribution (right) to finish the calculated time increment

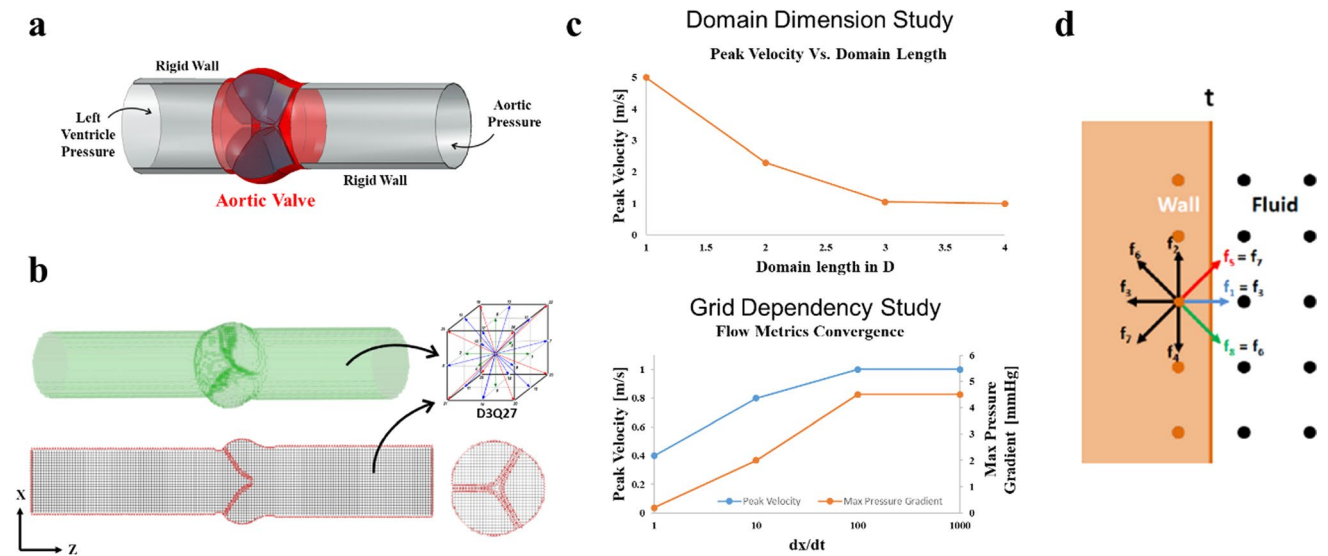


**Fig. 4** **a** Schematic view of the physical domain of fluid–structure interaction model, **b** 3D (upper) and section view (lower) of the numerical domain of FSI model using uniform distribution of unity D3Q27 lattices, **c** the effect of the physical domain length on the peak

velocity (upper) and grid dependency study examining the effect of the spatial to temporal ratio on the peak velocity and max pressure gradient (lower), **d** schematic demonstration of the used bounce-back boundary condition

**2.2.2 Temporal and spatial discretization sensitivity study:**

The FSI simulation's fluid domain in XFlow utilizes a uniform lattices grid. A grid independence study was conducted for the FSI simulation fluid domain, where the peak velocity and max pressure gradient metrics convergence were used to calculate the optimal lattice size. No local grid refinement was needed in the aortic root or the leaflets region of interest. Since the solver is transient and compressible and due to the nature of the LBM scheme employed, the information (pressure waves) naturally

travels at the numerical speed of sound  $C_{s_{numerical}}$  that were calculated according to:

$$C_{s_{numerical}} = \frac{dx}{\sqrt{3}dt} \tag{1}$$

where  $dx$  is the resolution at a given lattice level and  $dt$  is the associated time step for the same lattice level. For that reason, the numerical speed of sound should not exceed the flow thermodynamic speed of sound to prevent pressure waves in the domain. Therefore, the time step  $dt$  was set to satisfy:

$$C_{s_{\text{Thermodynamics}}} = C_{s_{\text{numerical}}} \rightarrow dt = \frac{dx}{\sqrt{3}C_{s_{\text{Thermodynamics}}}} \quad (2)$$

Hence, the spatial and temporal resolution ratio was fixed  $\frac{dt}{dx} = 100$  according to the sensitivity study (Fig. 4c). Moreover, mean flow values including stroke volume ( $\sim 70$  mL), cardiac output ( $\sim 5$  L/min) and mean velocity ( $\sim 0.5$  m/s) were calculated.

### 2.2.3 The numerical model

The flow simulation was discretized with  $\sim 1$  M unity D3Q27 lattices ( $84 \times 84 \times 155$ ) with high number of degrees of freedom per discrete element of fourth-order spatial discretization (Fig. 4b). The coarsest spatial length of 1 mm and a temporal 0.05 ms resolution of a constant time step were resolved according to the grid sensitivity study (Fig. 4c). Given our main interest in predicting large-scale features, the flow was assumed laminar. Expected differences due to the adoption of a turbulence model would have only a marginal effect on the current study and its relevance from the biomechanical point of view (Halevi et al. 2016). The blood was treated as a Newtonian and isothermal at a temperature of 37 °C with a dynamic viscosity of 0.0035 Pa and a density of 1050 kg/m<sup>3</sup> (Marom et al. 2012a). Time-dependent normotensive physiological pressure amplitude boundary conditions were applied on both sides of the domain as outlets pressure boundary conditions to minimize the inherent nature of pressure waves when using LBM. All other surfaces of the fluid domain were set as wall boundary conditions. This step provides the value of the following unknown particle distribution function created after the streaming step. Additionally, the bounce-back method

was used to impose a no-slip condition in the vicinity of the walls, applied after streaming (Chen et al. 2013).

### 2.2.4 FSI setup

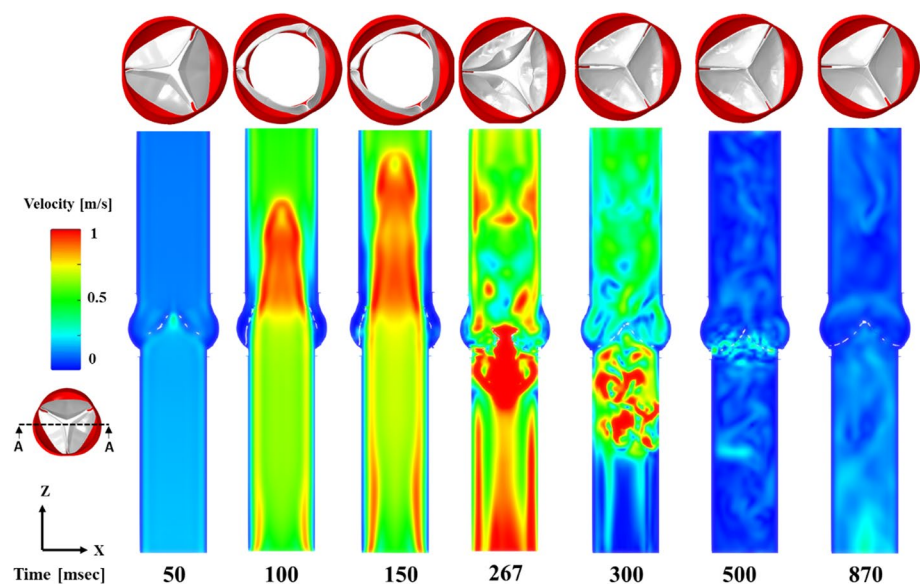
The FSI simulation was solved by a partitioned approach with a two-way coupling utilizing the XFlow and Abaqus (Dassault Systemes, Simulia Corp., Providence, RI) solvers for the fluid and structure, respectively. SIMULIA Co-Simulation Engine (Dassault Systemes, Simulia Corp., Providence, RI) managed the data transfer between the solvers. The explicit flow solver directly solves the flow equations and transfers the traction load on the leaflets, including fluid pressure and shear stress, to the structural solver. The implicit structural solver calculates the displacements by iteration until convergence and transfers the new geometry back to the flow solver. This process is repeated all over again for each step until the end of the simulation. The simulations were performed on a local workstation with Intel(R) Core(TM) i9-10980XE CPU @ 3.00 GHz. Eight cores were allocated for both solvers, each on its turn, and the simulation required  $\sim 75$  h to be solved. A master–slave contact algorithm was employed between the leaflets assuming a non-friction contact in the structural solver.

## 3 Results

### 3.1 Flow field

Figure 5 presents the flow velocity field evolution using FSI LBM-FE at representative time instants for TAV on the XZ symmetry plane and the corresponding variation of the EOA. At the beginning of the systole phase (50 ms) the flow field

**Fig. 5** FSI models using coupled LBM-FE: flow velocity at representative time points during TAV cardiac cycle



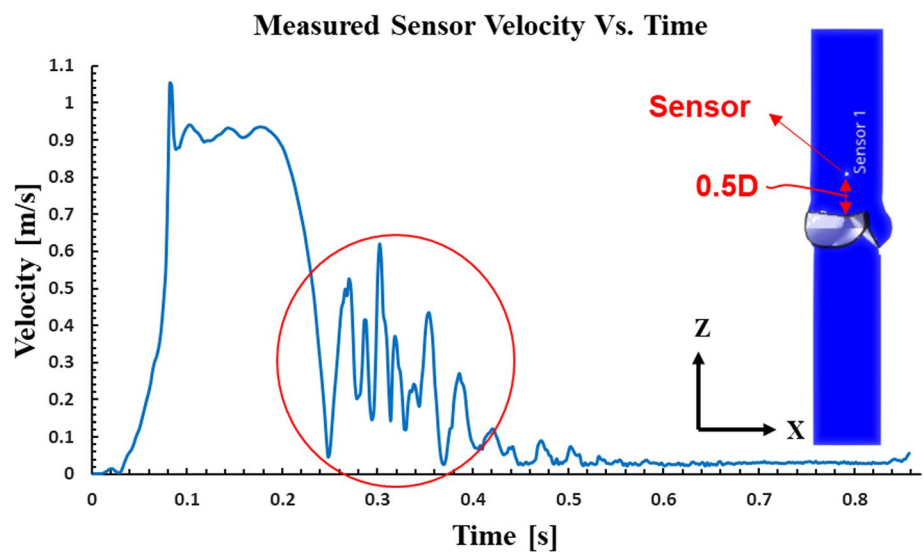
starts to develop and peaks during the systole peak phase (100 ms), with the flow characterized as a symmetric central jet flow with a maximum 1.00 m/s jet velocity. Toward the end of the systole phase (267 ms), a backward flow due to pressure decrease results in leaflets' partial to complete closure at the end of the systole (300 ms). Throughout this period, because the fluid is forced to change direction or stop abruptly, a pressure surge propagates through the valve and velocity fluctuations are observed. At the diastolic phase of the cardiac cycle (300–870 ms) the velocity drops approximately to zero through decaying small flow fluctuations, specifically at mid-diastole phase (500 ms). Accordingly, the EOA, which is directly affected by the flow field, increases from the early systolic phase (50 ms), to its peak during the

systole peak phase (100 ms), then decreasing gradually until leaflets' full closure at the end of systole (300 ms).

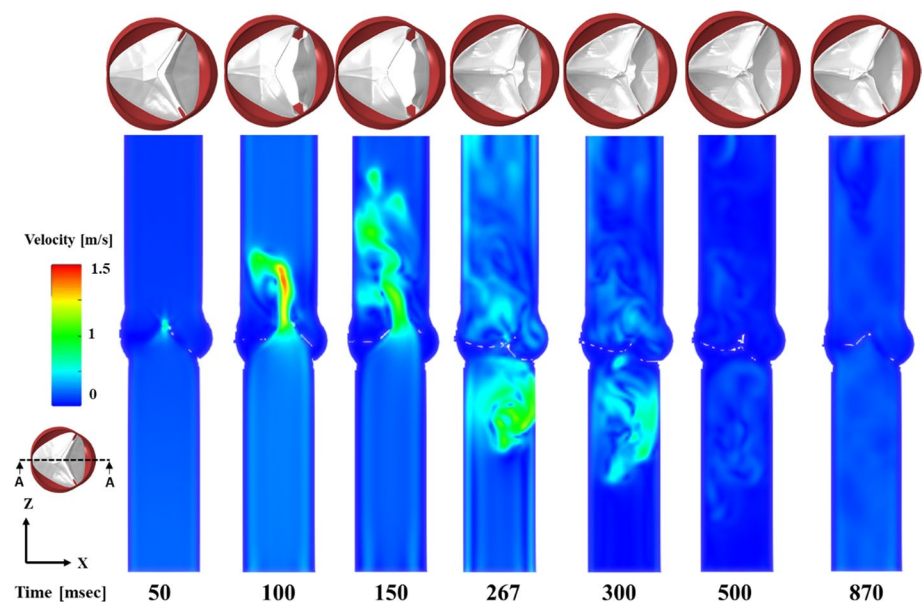
The evolution of the velocity was quantified at a representative point in the vicinity of the valve (0.5 diameter distance above the leaflets' coaptation on the XZ symmetry plane) as shown in Fig. 6. The velocity profile increases gradually until its peak at peak systole and decreases afterward. In between, starting with the leaflets partial closure, diastolic flow oscillations are distinctly captured until the complete decay toward the end of the cardiac cycle (seen in red in Fig. 6).

Figure 7 presents the flow velocity field evolution using FSI LBM-FE at representative time instants for BAV. At the beginning of the systole phase (50 ms) the flow field starts to develop and peaks during the systole peak phase

**Fig. 6** TAV velocity field through the cardiac cycle at XZ symmetry plane quantified at 0.5D height from the cusps' tip for LBM-FE FSI model. In red: diastolic velocity oscillations phenomenon which is explicitly observed using LBM-FE FSI model



**Fig. 7** FSI models using coupled LBM-FE: flow velocity at representative time points during BAV cardiac cycle



(100 ms), where the flow is characterized as an asymmetric jet flow with a maximum of 1.50 m/s jet velocity. Toward the end of the systole phase (267 ms) the pressure decrease creates a backward flow, resulting in the leaflets' partial until complete closing at the end of systole (300 ms). The closing phase is asynchronous because of the BAV morphology that mainly blocks the backward vortices and diverts them to the NFC side. At the diastolic phase of the cardiac cycle (300–870 ms), the velocity drops approximately to zero with no fluctuations. Accordingly, the EOA, which is partial and asymmetric in BAV, increases from the systole early start (50 ms), peaking during the systole peak (100 ms) and decreasing gradually until the leaflets' full closure at the end of systole (300 ms).

### 3.2 Mechanical stresses distribution

The maximum principal stresses are shown from the aortic view at systole peak for the cusps only and in addition for the CFN at mid-diastole—for both the TAV and BAV models (Fig. 8). For the TAV, the maximum principal stresses in the cusps are developing moderately  $\sim 10$  kPa around the leaflets' contact edges at systole peak, with maximum principal stresses of  $\sim 270$  kPa that are developing dominantly symmetrically along the leaflets' belly at mid-diastole. Similarly, for the BAV, maximum principal stresses  $\sim 80$  kPa are developing around the leaflets' contact edges and mainly on the raphe region at systole peak. Maximum principal stresses of  $\sim 300$  kPa are developing along the leaflets' belly at mid-diastole on the NFC and in the vicinity of the raphe on the FC. Yet, in the CFN, the fibers play a negligible role

in both models during the systole, and the developed stresses are concentrated mainly in the cusps. For that reason, we focused on the stresses developing in the CFN during the mid-diastolic phase where the leaflets' coaptation causes highly induced mechanical contact and hence increased stresses. The developed stresses in the CFN with a maximum value of  $\sim 3$  MPa are elevated during this period and are three orders of magnitude larger than those developed in the cusps—for both models.

### 3.3 Wall shear stress distribution

Figure 9 describes the wall shear stress (WSS) distribution from ventricular view at systole peak and mid-diastole, as it is well established that the unidirectional flow during these phases is prone to generate higher WSS more than caused by the recirculating flow on the aortic side (Thubrikar 1990). WSS magnitude of  $\sim 1$  Pa at systole peak and mid-diastole is observed for the TAV. At the systole peak, the WSS is higher around the coaptation of the leaflets and decreases gradually toward the belly and is more uniformly distributed along the leaflets' surface at mid-diastole due to the small velocity fluctuations. However, for BAV, WSS magnitude of  $\sim 1$  Pa at systole peak is observed where low WSS at mid-diastole was perceived.

## 4 Discussion

This study used the LBM-FE method to perform FSI simulations of AV dynamics with an embedded collagen fiber network in TAV and BAV models. The flow patterns and

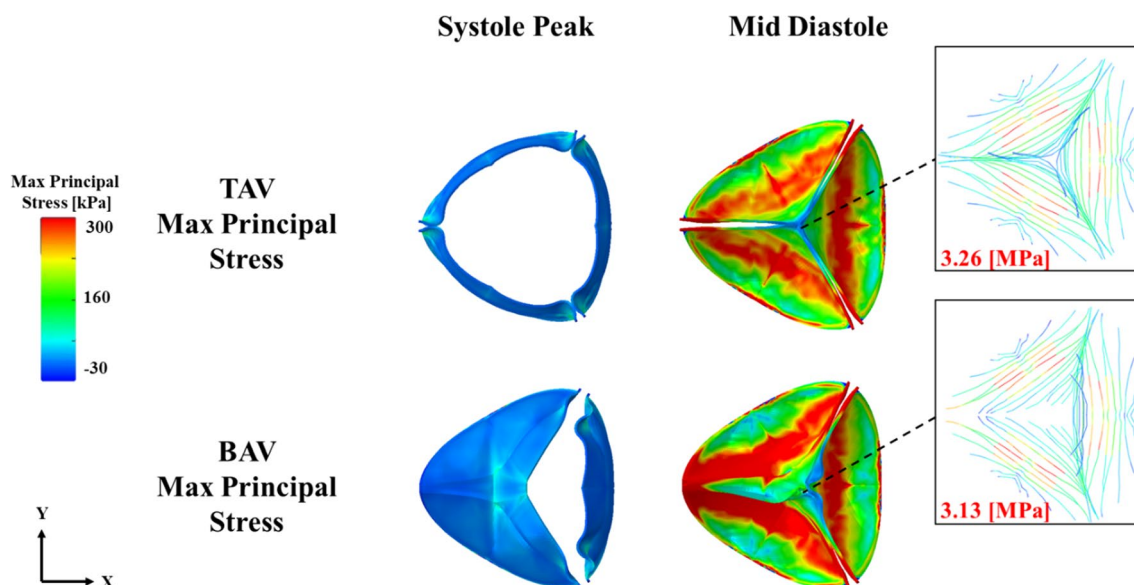
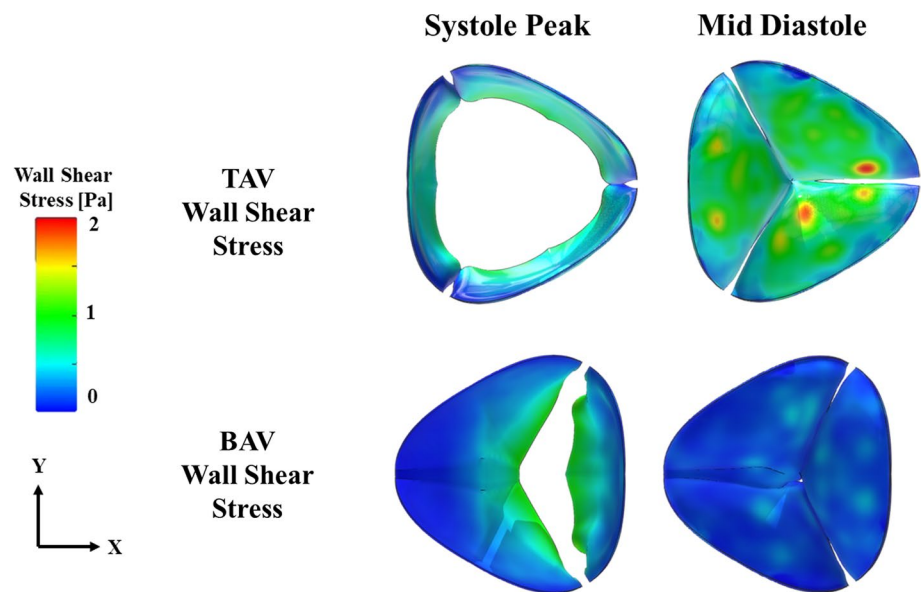


**Fig. 8** Maximum principal stress distributions (aortic side view) at peak systole and mid-diastole on TAV (upper row) and BAV (lower row) cusps with zoom on the collagen fiber network



**Fig. 9** Flow wall shear stress distributions (ventricles side view) at peak systole and mid-diastole on TAV (upper row) and BAV (lower row) cusps



the structural responses were analyzed and presented. By comparing the LBM-FE models' hemodynamic and heterogeneous structure anisotropic behavior with the available data from the literature, we aim to examine these LBM-FE models suitability for AV biomechanics simulations.

FSI analyses for TAV and BAV models were utilized and presented. Figure 5 illustrates TAV flow field patterns where the EOA at systole peak was calculated and found to be  $3.38 \text{ cm}^2$ , developing a max jet velocity of  $1.0 \text{ m/s}$ . The flow pattern appeared parabolic and central. The peak velocity and EOA adequately correspond to the published range of values in the literature ( $0.9\text{--}2.3 \text{ m/s}$ ) from *in vivo* (Mirabella 2014; Mahadevia et al. 2014; Rodríguez-Palomares et al. 2018), *in vitro* (Yap et al. 2011; Saikrishnan et al. 2012; McNally et al. 2017), *in silico* (FSI and CFD) (De Hart 2003; Kuan and Espino 2015; Mei et al. 2016; Cao et al. 2017; de Oliveira et al. 2020) studies and clinical guides (Akins et al. 2008; Grimard and Larson; Baumgartner et al. 2009). The predicted maximal principal stresses along the surface of the leaflets (Fig. 8 upper row) are concentrated around the belly region at the systole peak ( $\sim 10 \text{ kPa}$ ) and are elevated at mid-diastole, mainly sustained by the CFN. The values of the stresses cannot be verified and are assumed to be directly affected by the different validated metrics of the flow field and the EOA. WSS of  $\sim 1 \text{ Pa}$  is generated around the leaflets' coaptation region and gradually decreases toward the belly at the systole peak. However, during mid-diastole a uniform distribution of the same value is observed under the coaptation region (Fig. 9 upper row). Exploring the LBM-FE flow field (Fig. 5), it can be seen that the vortices on the ventricular side need more time to decay distal to the sinuses, increasing the WSS at mid-diastole near

the leaflets' surface. The WSS using LBM-FE falls within the expected range of values ( $0.43\text{--}5.0 \text{ Pa}$ ) reported in the literature from *in vivo* (Barker et al. 2012; Rodríguez-Palomares et al. 2018) and *in silico* (FSI and CFD) (Cao et al. 2017; Liu et al. 2018) studies.

A BAV model was studied as a test case of a pathological valve with irregular geometry; the flow field patterns and velocities (Fig. 7), mechanical stresses (Fig. 8 lower row) and WSS (Fig. 9 lower row) were examined. The BAV morphology led to partial opening during the systole. The EOA at the systole peak was calculated and found to be far smaller more than in TAV ( $1.19 \text{ vs. } 3.38 \text{ cm}^2$ ), and consequently, the developed jet had a greater maximum velocity as compared to the TAV ( $1.50 \text{ vs. } 1.0 \text{ m/s}$ ). The flow pattern appeared asymmetric and eccentric, and tilted toward the NFC wall side. Utilizing LBM-FE, the BAV model developed a higher jet velocity and a smaller EOA as expected compared to TAV (de Oliveira et al. 2020). At the systole peak, the maximal principal stresses along the surface of the leaflets were concentrated around the belly and raphe regions ( $\sim 80 \text{ kPa}$ ). At mid-diastole, the raphe formed a protruding bulk that blocked the backward flow, causing a higher leaflets' resistance for the leaflets closure dynamics. Hence, the mechanical stresses in BAV were slightly higher more than in TAV ( $300 \text{ kPa vs. } 270 \text{ kPa}$ ). Furthermore, the WSS at systole peak reached a high value around the leaflets' coaptation region that gradually decreases to zero toward the belly of the FC. At mid-diastole the WSS was almost negligible. Unlike the WSS in the TAV, the FC geometry partially blocked the backward vorticity in the closing phase and led to their faster decay, resulting with a lower WSS in the BAV at mid-diastole as compared to the TAV.

Consequently, the significance of the instantaneous mesoscale data using LBM-FE, both for structural and the flow field, is exemplified by inspecting the BAV closure phase. From the structural and AV kinematics point of view, the leaflets reach a complete closure immediately following the end of the systolic phase, the same as expected for TAV. Despite its asymmetric morphology, non-stenotic BAV is expected to reach full closure even though asynchronously and not suffer from regurgitation (Mendi et al. 2020). The closing phase in asymmetrical morphology as BAV is a very fine process numerically, which could face instabilities and divergences in the closing phase (Lavon et al. 2018). This fine closing contact is explicitly captured by utilizing LBM-FE, based on the local instantaneous solution.

The FSI simulations are utilized to investigate the AV behavior and allow for exploring different geometry, material and interaction factors. The comparison of the hemodynamic metrics to the literature is used to confirm some of the predictions provided by the FSI models and thus testify their overall reliability. Given that the hemodynamic metrics and the structural responses have reciprocal interplay, this plays a major role in determining the accuracy of the stresses on the leaflets and sufficiently support the reliability of the results in the absence of *in vivo* experimental data. Therefore, the suggested anisotropic heterogeneous model of the AV leaflets better represents its anatomical structure and the developed predicted stresses. Furthermore, the CFN is responsible for stabilizing and positioning of the leaflets, sustaining the load during the valve's opening and closing phases. The maximum principal stresses in the leaflet elastin matrix are significantly reduced both for tensile and compressive stresses, where the CFN carries most of the load. This appears in all the parts of the leaflets, where the collagen bundles are much stiffer more than the surrounding soft tissue; they would carry most of the stress in the specific bundle orientation. The maximum stress magnitudes in the CFN during diastole are significantly higher more than during systole by orders of magnitude as compared to those of the elastin matrix. The advanced modeling technique, both for the structure that include the CFN and the fluid, reveals the importance of accurate tissue modeling to simulate its hemodynamic performance. It can also guide how to achieve better load distribution in prosthetic aortic valve design for example.

From the hemodynamics point of view, the diastolic velocity oscillations phenomenon, related to late systolic leaflets vibrations, is well captured by using the LBM-FE FSI. This phenomenon occurs when there is rapid retardation of the flow with the closure of the aortic valve. In the aorta, significant regurgitation of the blood flow transpires during the valve closure and gradually decelerates, until it totally vanishes (approximately between 200 and 350 ms of the cardiac cycle). This causes a high fluid momentum to be

propagated backward along the aorta, which interacts with the compliant leaflets and generates large oscillations in the velocity (Bluestein and Einav 1993, 1994, 1995; Moore and Dasi 2014; Lee et al. 2020). These oscillations were numerically quantified at a representative point in the vicinity of the valve (0.5 diameter distance above the leaflets' coaptation on the XZ symmetry plane), as can be seen in red in Fig. 6. It demonstrates that the diastolic flow oscillations are distinctly captured using the LBM-FE FSI approach. This phenomenon's highly transient nature further supports utilizing the LBM-FE FSI approach that is better suited for capturing such fast oscillations.

Regarding numerical discretization, no adaptive and local grid refinement during the solution in LBM-FE approach was needed to capture the global or local hemodynamic metrics. The unvaried determined grid by the mesh study in Fig. 4c was suitable for each interval of the solution. In contrast, when using a traditional finite volume approach, during the solution a dynamically adaptive local refinement near the walls and the moving parts is usually utilized [38]. Using a uniform grid through the LBM-FE FSI solution shortens the initial post-processing procedure, reduces computer resources during the incremental solution and easily handles complicated geometries.

## 5 Limitations

This study has several limitations which should be considered when interpreting the results. Healthy material properties were assumed for the BAV FE model because of the lack of experimental data for BAV valves and specifically the raphe region. Furthermore, the initial simulation conditions were assumed for an almost closed valve with no residual stresses in the tissue. This assumption is based on prior studies showing reasonable behavior of the overall kinematics (Marom et al. 2012a; Lavon et al. 2018). Regarding the flow regime, the LBM can be viewed as a direct numerical simulation (DNS) method for solving fluid flow (Chikatamarla et al. 2010). Turbulent results are expected to emerge from the proposed LBM modeling when one resolves all scales in the flow with the proper refinement. A refined mesh to the mentioned scale can be qualified as a DNS. Our LBM model does not qualify (a mesh of many millions of elements is needed). The aim was to perform FSI simulation that strikes a balance between the structural and fluid grids yet be able to carry the simulation for the entire cardiac cycle. To perform advanced DNS-FSI modeling requires a highly refined and computationally intensive computational grid able to resolve all the scales. In addition, it can be argued that turbulence models are needed. The flow regime in the LBM models is in the laminar-transitional field and intermittently turbulent

only. Moreover, studies have raised doubts regarding the benefits of applying turbulent models for aortic valve FSI modeling, compared with the inaccuracy cost of laminar assumption (Yoganathan et al. 2005; Cao and Sucosky 2017; Zhang and Zhang 2018; de Oliveira et al. 2020). Therefore, in our case, the turbulence model might not result in considerably improved outcomes compared with the laminar assumption.

Moreover, the FSI simulation should be further improved by modeling the entire heart geometry where the LV and the aorta dynamic responses directly affect the aortic root and leaflets' kinematics, and as a result the hemodynamic response (Morany et al. 2021). Finally, this research focuses on a numerical study rather than experimental or clinical measurements. The above-mentioned results were compared to previously published numerical models, and the conclusions focus on a comparative study rather than absolute values.

### 6 Conclusions

A new FSI framework integrating the LBM-FE is presented and used for the analysis of TAVs and BAVs. The coupled LBM-FE FSI is very effective and yields good correlations with existing resolved results reported in the literature. We have shown that LBM-FE FSI model can predict the flow and structural properties of TAV, and adequately handles irregular geometries such as BAV. The dynamic behavior of the flow has been captured, providing vital information on the flow structure and their transient nature. The significance of the stress distribution and the interplay between the CFN and the elastin matrix in the leaflet through the cardiac cycle is demonstrated. The coupled LBM-FE FSI framework of the structural and the flow behaviors, that bridges the cross-scales of the AV, has a potential to produce new insights into its complex multi-scale dynamics.

### Appendix A

The LBM algorithm and method are derived from the Boltzmann transport equation:

$$\frac{\partial f}{\partial t} + \mathbf{e} \cdot \nabla f = \Omega \tag{3}$$

where  $f = f(x, t, \mathbf{e})$  is a particle distribution function that depends on space vector  $\mathbf{x}$ , time  $t$ , velocity direction unit  $\mathbf{e}$  and the collision operator  $\Omega$ . The equation describes the evolution of a rarefied gas by means of one-particle distribution function, under the assumption that only two particle collisions happen in a time interval and the particles lacking

a mutual relationship or connection before the collision. The Boltzmann equation is discretized with each discrete  $\mathbf{e}_i$  velocity and on the lattice:

$$f_i(\mathbf{r} + \mathbf{e}_i, t + dt) = f_i(\mathbf{r}, t) + \Omega_i(f_1, \dots, f_b) \tag{4}$$

The macroscopic variables, mass and momentum, can be derived from the statistical moment of the particle density function  $f$  as follows:

$$\rho = \sum_{i=1}^b f_i, \quad \rho \mathbf{v} = \sum_{i=1}^b f_i \mathbf{e}_i \tag{5}$$

The collision operator models the particle collision step and based on the relaxation of the particle distribution function toward the equilibrium state. The proposed collision operator is the multi-relaxation time (MRT) suggested by D'Humières et al. (2002). This operator relaxes each moment individually and calculates the moments according to central momentum space. In the mathematical form, the equilibrium state  $f^{eq}$  is set according to Maxwell–Boltzmann distribution:

$$f^{eq}(x, \xi, t) = \frac{\rho}{(2\pi RT)^{3/2}} \exp \left[ -\frac{(\xi - u)^2}{2RT} \right] \tag{6}$$

and obtained by a truncated small velocity expansion of often called low Mach number approximation by 2nd-order Taylor series:

$$f_i^{eq} = \rho w_i \left( 1 + \frac{e_{i\alpha} u_\alpha}{c_s^2} + \frac{u_\alpha u_\beta}{2c_s^2} \left( \frac{e_{i\alpha} e_{i\beta}}{c_s^2} - \delta_{\alpha\beta} \right) \right) \tag{7}$$

where  $w_i$  are weighting constants built to preserve the isotropy,  $c_s$  is the speed of sound,  $R$  is the ideal gas constant,  $T$  is the temperature where  $c_s^2 = RT$ ,  $u$  is the macroscopic velocity,  $\xi$  is the microscopic velocity of a particle,  $\delta$  is the Kronecker delta,  $\alpha$  and  $\beta$  sub-indexes denote the different spatial components of the vectors appearing in the equation and Einsteins' summation convention over repeated indices have been used. Analogically to Eqs. (3), the raw moment  $\mu$  of the particle distribution function  $f$  can be expressed in a more general form by the relation:

$$\mu_{x^k y^l z^m} = \sum_{i=1}^b f_i e_{ix}^k e_{iy}^l e_{iz}^m \tag{8}$$

where  $k, l, m$  are, respectively, the orders of moments taken in  $x, y, z$  directions. Denoting  $\mu_i$  as a raw moment  $\mu_{x^k y^l z^m}$  of a given combination of  $(k, l, m)$ , the relation between the particle distribution functions and the raw moments can be expressed in the following matrix form using the transformation matrix  $M_{ij}$ :

$$\mu_i = M_{ij} f_j \tag{9}$$

MRT collision operator can be calculated as a relaxation in momentum space followed by the inverse transformation to distribution function space:

$$\Omega_i^{\text{MRT}} = -M_{ij}^{-1} S_{ij} (\mu_i^{\text{eq}} - \mu_i) \quad (10)$$

where  $S_{ij}$  is the diagonal relaxation matrix and  $\mu_i^{\text{eq}}$  is the raw moment at equilibrium. Once the post-collision  $\mu_i$  is obtained, its particle distribution function can be recovered from inverse transformation matrix:

$$f_j = -M_{ij}^{-1} \mu_i \quad (11)$$

The WSS using the LBM was computed using the shear rate relation  $\tau = \mu \dot{\gamma}$ , where the shear rate  $\dot{\gamma}$  is obtained through the derivatives of the velocity field:

$$\dot{\gamma} = \text{sqrt} \left\{ \left[ \frac{\partial u}{\partial x} \left( \frac{\partial u}{\partial x} + \frac{\partial u}{\partial x} \right) + \frac{\partial u}{\partial y} \left( \frac{\partial u}{\partial y} + \frac{\partial v}{\partial x} \right) + \frac{\partial u}{\partial z} \left( \frac{\partial u}{\partial z} + \frac{\partial w}{\partial x} \right) \right] + \left[ \frac{\partial v}{\partial x} \left( \frac{\partial v}{\partial x} + \frac{\partial u}{\partial y} \right) + \frac{\partial v}{\partial y} \left( \frac{\partial v}{\partial y} + \frac{\partial v}{\partial y} \right) + \frac{\partial v}{\partial z} \left( \frac{\partial v}{\partial z} + \frac{\partial w}{\partial y} \right) \right] + \left[ \frac{\partial w}{\partial x} \left( \frac{\partial w}{\partial x} + \frac{\partial u}{\partial z} \right) + \frac{\partial w}{\partial y} \left( \frac{\partial w}{\partial y} + \frac{\partial v}{\partial z} \right) + \frac{\partial w}{\partial z} \left( \frac{\partial w}{\partial z} + \frac{\partial w}{\partial z} \right) \right] \right\}$$

**Acknowledgements** XFlow SIMULIA is in academic partnerships with Prof. RHA and Prof. DB. AM acknowledges the support of the Planning and Budgeting Committee–Israeli Council for Higher Education. RHA gratefully acknowledges the support of the Nathan Cummings Chair in Mechanics.

**Author contributions** A.M.: conceptualization, data curation, formal analysis, methodology, software, visualization, writing—original draft. K.L.: conceptualization, writing—review & editing. R.B.: conceptualization, software, visualization. B.K.: conceptualization, writing—review & editing. A.H.: conceptualization, writing—review & editing. D.B.: conceptualization, funding acquisition, methodology, writing—review & editing. R.H.A.: conceptualization, funding acquisition, methodology, resources, software, supervision, visualization, writing—review & editing. All authors gave final approval for publication and agreed to be held accountable for the work performed therein.

**Funding** This study was funded by a National Institute of Health grant: Bioengineering Research Partnerships (U01) under Grant No. EB026414.

## Declarations

**Conflict of interest** Karin Lavon is an employee of Edwards Lifesciences Ltd. Author Danny Bluestein has an equity interest in Polynova Cardiovascular Inc. All other authors state that they have no financial and/or personal relationships with other people or organizations that could inappropriately influence or bias the publication of this study.

## References

Abbas SS, Nasif MS, Al-Waked R (2022) State-of-the-art numerical fluid–structure interaction methods for aortic and mitral heart

- valves simulations: a review. *SIMULATION* 98:3–34. <https://doi.org/10.1177/00375497211023573>
- Akins CW, Travis B, Yoganathan AP (2008) Energy loss for evaluating heart valve performance. *J Thorac Cardiovasc Surg* 136:820–833
- Barker AJ, Markl M, Bürk J et al (2012) Bicuspid aortic valve is associated with altered wall shear stress in the ascending aorta. *Circ Cardiovasc Imaging* 5:457–466. <https://doi.org/10.1161/CIRCI-MAGING.112.973370>
- Baumgartner H, Hung J, Bermejo J et al (2009) Echocardiographic assessment of valve stenosis: european association of echocardiography (EAE)/american society of echocardiography (ASE) recommendations for clinical practice. *Eur J Echocardiogr* 10:1–25
- Bernsdorf J, Brenner G, Durst F (2000) Numerical analysis of the pressure drop in porous media flow with lattice Boltzmann (BGK) automata. *Comput Phys Commun* 129:247–255
- Bluestein D, Einav S (1993) Spectral estimation and analysis of LDA data in pulsatile flow through heart valves. *Exp Fluids* 15:341–353
- Bluestein D, Einav S (1994) Transition to turbulence in pulsatile flow through heart valves—a modified stability approach. *J Biomech Eng* 116:477–487. <https://doi.org/10.1115/1.2895799>
- Bluestein D, Einav S (1995) The effect of varying degrees of stenosis on the characteristics of turbulent pulsatile flow through heart valves. *J Biomech* 28:915–924. [https://doi.org/10.1016/0021-9290\(94\)00154-V](https://doi.org/10.1016/0021-9290(94)00154-V)
- Bongert M, Wüst J, Geller M, et al (2018) Comparison of two biological aortic valve prostheses inside patient-specific aorta model by bi-directional fluid–structure interaction. 4:59–62
- Borzajani I, Ge L, Sotiropoulos F (2010) High-resolution fluid–structure interaction simulations of flow through a bi-leaflet mechanical heart valve in an anatomic aorta. *Ann Biomed Eng* 38:326–344. <https://doi.org/10.1007/s10439-009-9807-x>
- Boyd J, Buick JM, Cosgrove JA, Stansell P (2004) Application of the lattice Boltzmann method to arterial flow simulation: investigation of boundary conditions for complex arterial geometries. *Australas Phys Eng Sci Med* 27:207–212
- Cao K, Sucusky P (2017) Computational comparison of regional stress and deformation characteristics in tricuspid and bicuspid aortic valve leaflets. *Int J Numer Method Biomed Eng*. <https://doi.org/10.1002/cnm.2798>
- Cao K, Atkins SK, McNally A et al (2017) Simulations of morphotype-dependent hemodynamics in non-dilated bicuspid aortic valve aortas. *J Biomech* 50:63–70. <https://doi.org/10.1016/j.jbiomech.2016.11.024>
- Cedars A, Braverman AC (2012) The many faces of bicuspid aortic valve disease. *Prog Pediatr Cardiol* 34:91–96. <https://doi.org/10.1016/j.ppedcard.2012.08.006>
- Chandra S, Rajamannan NM, Sucusky P (2012) Computational assessment of bicuspid aortic valve wall-shear stress: implications for calcific aortic valve disease. *Biomech Model Mechanobiol* 11:1085–1096
- Chen Y, Luo H (2018) A computational study of the three-dimensional fluid–structure interaction of aortic valve. *J Fluids Struct* 80:332–349
- Chen L, Yu Y, Hou G (2013) Sharp-interface immersed boundary lattice Boltzmann method with reduced spurious-pressure oscillations for moving boundaries. *Phys Rev E Stat Nonlinear Soft Matter Phys* 87:1–11. <https://doi.org/10.1103/PhysRevE.87.053306>
- Chikatamarla SS, Frouzakis CE, Karlin IV et al (2010) Lattice Boltzmann method for direct numerical simulation of turbulent flows. *J Fluid Mech* 656:298–308. <https://doi.org/10.1017/S0022112010002740>
- Conti CA, Della Corte A, Votta E et al (2010a) Biomechanical implications of the congenital bicuspid aortic valve: a finite element study of aortic root function from in vivo data. *J Thorac Cardiovasc Surg* 140:890–896.e2

- Conti CA, Votta E, Della Corte A et al (2010b) Dynamic finite element analysis of the aortic root from MRI-derived parameters. *Med Eng Phys* 32:212–221
- Davies PF (2009) Hemodynamic shear stress and the endothelium in cardiovascular pathophysiology. *Nat Clin Pract Cardiovasc Med* 6:16–26
- de Oliveira DMC, Abdullah N, Green NC, Espino DM (2020) Biomechanical assessment of bicuspid aortic valve phenotypes: a fluid-structure interaction modelling approach. *Cardiovasc Eng Technol* 11:431–447. <https://doi.org/10.1007/s13239-020-00469-9>
- D’Humières D, Ginzburg I, Krafczyk M et al (2002) Multiple-relaxation-time lattice Boltzmann models in three dimensions. *Philos Trans A Math Phys Eng Sci* 360:437–451
- Dorschner B, Chikatamarla SS, Karlin IV (2018) Fluid-structure interaction with the entropic lattice Boltzmann method. *Phys Rev E* 97:1–12
- Dua MM, Dalman RL (2010) Hemodynamic Influences on abdominal aortic aneurysm disease: application of biomechanics to aneurysm pathophysiology. *Vascul Pharmacol* 53:11–21. <https://doi.org/10.1016/j.vph.2010.03.004>
- Fang H, Wang Z, Lin Z, Liu M (2002) Lattice Boltzmann method for simulating the viscous flow in large distensible blood vessels. *Phys Rev E Stat Nonlinear, Soft Matter Phys* 65:1–11
- Fukui T, Morinishi K (2013) Blood flow simulation in the aorta with aortic valves using the regularized lattice boltzmann method with LES model. *WIT Trans Built Environ* 129:97–107
- Gao B, Zhang Q (2020) Biomechanical effects of the working modes of LVADs on the aortic valve: a primary numerical study. *Comput Methods Programs Biomed.* <https://doi.org/10.1016/j.cmpb.2020.105512>
- Gao B, Zhang Q, Chang Y (2019) Hemodynamic effects of support modes of LVADs on the aortic valve. *Med Biol Eng Comput* 57:2657–2671. <https://doi.org/10.1007/s11517-019-02058-y>
- Ge L, Jones SC, Sotiropoulos F et al (2003) Numerical simulation of flow in mechanical heart valves: grid resolution and the assumption of flow symmetry. *J Biomech Eng* 125:709
- Ghosh R, Marom G, Rotman O et al (2018) Comparative fluid-structure interaction analysis of polymeric transcatheter and surgical aortic valves’ hemodynamics and structural mechanics. *J Biomech Eng* 140:1–10
- Ghosh RP, Marom G, Bianchi M et al (2020) Numerical evaluation of transcatheter aortic valve performance during heart beating and its post-deployment fluid–structure interaction analysis. *Biomech Model Mechanobiol.* <https://doi.org/10.1007/s10237-020-01304-9>
- Grimard BH, Larson JM (2008) Aortic stenosis: diagnosis and treatment. *Am Fam Phys* 78:717–724
- Gundiah N, Kam K, Matthews PB et al (2008) Asymmetric mechanical properties of porcine aortic sinuses. *Ann Thorac Surg* 85:1631–1638
- Gunstensen AK, Rothman DH, Zaleski S, Zanetti G (1991) Lattice Boltzmann model of immiscible fluids. *Phys Rev A* 43:4320–4327
- Haj-Ali R, Dasi LP, Kim HS et al (2008) Structural simulations of prosthetic tri-leaflet aortic heart valves. *J Biomech* 41:1510–1519
- Haj-Ali R, Marom G, Ben Zekry S et al (2012) A general three-dimensional parametric geometry of the native aortic valve and root for biomechanical modeling. *J Biomech* 45:2392–2397
- Halevi R, Hamdan A, Marom G et al (2016) Fluid-structure interaction modeling of calcific aortic valve disease using patient-specific three-dimensional calcification scans. *Med Biol Eng Comput* 54:1683–1694
- Han-Taw C, Jae-Yuh L (1993) Numerical analysis for hyperbolic heat conduction. *Int J Heat Mass Transf* 36:2891–2898. [https://doi.org/10.1016/0017-9310\(93\)90108-I](https://doi.org/10.1016/0017-9310(93)90108-I)
- De Hart J (2003) A three-dimensional computational analysis of fluid-structure interaction in the aortic valve. *J Biomech* 36:103–112
- He X, Luo L-S (1997) Lattice Boltzmann model for the incompressible Navier-Stokes equation. *J Stat Phys* 88:927–944
- Hellmeier F, Nordmeyer S, Yevtushenko P et al (2018) Hemodynamic evaluation of a biological and mechanical aortic valve prosthesis using patient-specific MRI-based CFD. *Artif Organs* 42:49–57
- Jermihov PN, Jia L, Sacks MS et al (2011) Effect of geometry on the leaflet stresses in simulated models of congenital bicuspid aortic valves. *Cardiovasc Eng Technol* 2:48–56
- Katayama S, Umetani N, Hisada T, Sugiura S (2013) Bicuspid aortic valves undergo excessive strain during opening: a simulation study. *J Thorac Cardiovasc Surg* 145:1570–1576
- Kim YW, Moon JY, Li WJ et al (2020) Effect of membrane insertion for tricuspid regurgitation using immersed-boundary lattice Boltzmann method. *Comput Methods Programs Biomed* 191:105421. <https://doi.org/10.1016/j.cmpb.2020.105421>
- Krafczyk M, Cerrolaza M, Schulz M, Rank E (1998) Analysis of 3D transient blood flow passing through an artificial aortic valve by Lattice-Boltzmann methods. *J Biomech* 31:453–462
- Kuan MYS, Espino DM (2015) Systolic fluid-structure interaction model of the congenitally bicuspid aortic valve: assessment of modelling requirements. *Comput Methods Biomech Biomed Engin* 18(12):1305–1320
- Lai YG, Ching-Long Lin J (2001) Accuracy and efficiency study of lattice Boltzmann method for steady-state flow simulations. *Numer Heat Transf Part B Fundam* 39:21–43
- Lavon K, Halevi R, Marom G et al (2018) Fluid-structure interaction models of bicuspid aortic valves: the effects of nonfused cusp angles. *J Biomech Eng* 140:1–7. <https://doi.org/10.1115/1.4038329>
- Lee JH, Rygg AD, Kolahdouz EM et al (2020) Fluid-structure interaction models of bioprosthetic heart valve dynamics in an experimental pulse duplicator. *Ann Biomed Eng* 48:1475–1490. <https://doi.org/10.1007/s10439-020-02466-4>
- Liu Y (2012) A lattice Boltzmann model for blood flows. *Appl Math Model* 36:2890–2899
- Liu Y, Kasyanov V, Schoepfoerster RT (2007) Effect of fiber orientation on the stress distribution within a leaflet of a polymer composite heart valve in the closed position. *J Biomech* 40:1099–1106
- Liu J, Shar JA, Sucusky P (2018) Wall shear stress directional abnormalities in BAV aortas: toward a new hemodynamic predictor of aortopathy? *Front Physiol* 9:993. <https://doi.org/10.3389/fphys.2018.00993>
- Macmeccan RM, Clausen JR, Neitzel GP, Aidun CK (2009) Simulating deformable particle suspensions using a coupled lattice-Boltzmann and finite-element method. *J Fluid Mech* 618:13–39. <https://doi.org/10.1017/S0022112008004011>
- Mahadevia R, Barker AJ, Schnell S et al (2014) Bicuspid aortic cusp fusion morphology alters aortic three-dimensional outflow patterns, wall shear stress, and expression of aortopathy. *Circulation* 129:673–682. <https://doi.org/10.1161/CIRCULATIONAHA.113.003026>
- Marom G (2015) Numerical methods for fluid-structure interaction models of aortic valves. *Arch Comput Methods Eng* 22:595–620
- Marom G, Haj-Ali R, Raanani E et al (2012a) A fluid-structure interaction model of the aortic valve with coaptation and compliant aortic root. *Med Biol Eng Comput* 50:173–182
- Marom G, Haj-Ali R, Rosenfeld M et al (2013a) Aortic root numeric model: annulus diameter prediction of effective height and coaptation in post-aortic valve repair. *J Thorac Cardiovasc Surg* 145:9–11
- Marom G, Peleg M, Halevi R et al (2013b) Fluid-structure interaction model of aortic valve with porcine-specific collagen fiber

- alignment in the cusps. *J Biomech Eng* 135:1–6. <https://doi.org/10.1115/1.4024824>
- Marom G, Kim HS, Rosenfeld M, et al (2012b) Effect of asymmetry on hemodynamics in fluid-structure interaction model of congenital bicuspid aortic valves. In: Annual International Conference of the IEEE Engineering in Medicine and Biology Society EMBS 637–640
- Martínez DO, Chen S, Matthaeus WH (1994) Lattice Boltzmann magnetohydrodynamics. *Phys Plasmas* 1:1850–1867. <https://doi.org/10.1063/1.870640>
- Masri A, Svensson LG, Griffin BP, Desai MY (2017) Contemporary natural history of bicuspid aortic valve disease: a systematic review. *Heart* 103:1323–1330. <https://doi.org/10.1136/heartjnl-2016-309916>
- McNally A, Madan A, Sucusky P (2017) Morphotype-dependent flow characteristics in bicuspid aortic valve ascending aortas: a benchtop particle image velocimetry study. *Front Physiol* 8:44. <https://doi.org/10.3389/fphys.2017.00044>
- Mega M, Marom G, Halevi R et al (2016) Imaging analysis of collagen fiber networks in cusps of porcine aortic valves: effect of their local distribution and alignment on valve functionality. *Comput Methods Biomech Biomed Eng* 19:1002–1008
- Mei S, de Souza Júnior FSN, Kuan MYS et al (2016) Hemodynamics through the congenitally bicuspid aortic valve: a computational fluid dynamics comparison of opening orifice area and leaflet orientation. *Perfusion* 31:683–690. <https://doi.org/10.1177/0267659116656775>
- Mendi MOE, Turla FRS, Hosh RAMPG et al (2020) Patient-specific bicuspid aortic valve biomechanics : a magnetic resonance imaging integrated fluid—structure interaction approach. *Ann Biomed Eng*. <https://doi.org/10.1007/s10439-020-02571-4>
- Mirabella L (2014) MRI-based protocol to characterize the relationship between bicuspid aortic valve morphology and hemodynamics. *Ann Biomed Eng* 43:1815–1827
- Mirzaee H, Henn T, Krause MJ et al (2017) MRI-based computational hemodynamics in patients with aortic coarctation using the lattice Boltzmann methods: clinical validation study. *J Magn Reson Imaging* 45:139–146. <https://doi.org/10.1002/jmri.25366>
- Missirlis YF, Chong M (1978) Aortic valve mechanics—part I: material properties of natural porcine aortic valves. *J Bioeng* 2:287–300
- Moore B, Dasi LP (2014) SPATIO-temporal complexity of the aortic sinus vortex. *Exp Fluids* 55:1770. <https://doi.org/10.1007/s00348-014-1770-0>
- Morany A, Lavon K, Bluestein D et al (2021) Structural responses of integrated parametric aortic valve in an electro-mechanical full heart model. *Ann Biomed Eng* 49:441–454. <https://doi.org/10.1007/s10439-020-02575-0>
- Nestola MGC, Zulian P, Gaedke-Merzhäuser L, Krause R (2021) Fully coupled dynamic simulations of bioprosthetic aortic valves based on an embedded strategy for fluid-structure interaction with contact. *Europace* 23:I96–I104. <https://doi.org/10.1093/europace/eaab398>
- Ouared R, Chopard B, Stahl B et al (2008) Thrombosis modeling in intracranial aneurysms: a lattice Boltzmann numerical algorithm. *Comput Phys Commun* 179:128–131
- Pelliccioni O, Cerrolaza M, Herrera M (2007) Lattice Boltzmann dynamic simulation of a mechanical heart valve device. *Math Comput Simul* 75:1–14
- Rankin JS, Dalley AF, Crooke PS, Anderson RH (2008) A “hemispherical” model of aortic valvar geometry. *J Heart Valve Dis* 17:179–186
- Rodríguez-Palomares JF, Dux-Santoy L, Guala A et al (2018) Aortic flow patterns and wall shear stress maps by 4D-flow cardiovascular magnetic resonance in the assessment of aortic dilatation in bicuspid aortic valve disease. *J Cardiovasc Magn Reson* 20:28. <https://doi.org/10.1186/s12968-018-0451-1>
- Saikrishnan N, Yap C-H, Milligan NC et al (2012) In vitro characterization of bicuspid aortic valve hemodynamics using particle image velocimetry. *Ann Biomed Eng* 40:1760–1775. <https://doi.org/10.1007/s10439-012-0527-2>
- Sigüenza J, Pott D, Mendez S et al (2018) Fluid-structure interaction of a pulsatile flow with an aortic valve model: a combined experimental and numerical study. *Int J Numer Method Biomed Eng* 34:1–19
- Sun W, Abad A, Sacks MS (2005) Simulated bioprosthetic heart valve deformation under quasi-static loading. *J Biomech Eng* 127:905–914. <https://doi.org/10.1115/1.2049337>
- Tan J, Sinno TR, Diamond SL (2018) A parallel fluid-solid coupling model using LAMMPS and Palabos based on the immersed boundary method. *J Comput Sci* 25:89–100
- Thubrikar M (1990) The aortic valve/author, Mano Thubrikar. CRC Press Boca Raton, Fla
- Weese J, Lungu A, Peters J et al (2017) CFD-and Bernoulli-based pressure drop estimates: a comparison using patient anatomies from heart and aortic valve segmentation of CT images. *Med Phys* 44:2281–2292
- Wu MCH, Zakerzadeh R, Kamensky D et al (2018) An anisotropic constitutive model for immersogeometric fluid-structure interaction analysis of bioprosthetic heart valves. *J Biomech* 74:23–31
- Yap CH, Saikrishnan N, Yoganathan AP (2011) Experimental measurement of dynamic fluid shear stress on the ventricular surface of the aortic valve leaflet. *Biomech Model Mechanobiol* 11:231–244
- Yoganathan AP, Chandran KB, Sotiropoulos F (2005) Flow in prosthetic heart valves: state-of-the-art and future directions. *Ann Biomed Eng* 33:1689–1694
- Yun BM, Dasi LP, Aidun CK, Yoganathan AP (2014a) Computational modelling of flow through prosthetic heart valves using the entropic lattice-Boltzmann method. *J Fluid Mech* 743:170–201
- Yun BM, McElhinney DB, Arjunon S et al (2014b) Computational simulations of flow dynamics and blood damage through a bileaflet mechanical heart valve scaled to pediatric size and flow. *J Biomech* 47:3169–3177
- Zhang R, Zhang Y (2018) An experimental study of pulsatile flow in a compliant aortic root model under varied cardiac outputs. *Fluids*. <https://doi.org/10.3390/fluids3040071>

**Publisher's Note** Springer Nature remains neutral with regard to jurisdictional claims in published maps and institutional affiliations.

Springer Nature or its licensor (e.g. a society or other partner) holds exclusive rights to this article under a publishing agreement with the author(s) or other rightsholder(s); author self-archiving of the accepted manuscript version of this article is solely governed by the terms of such publishing agreement and applicable law.